

Cite this: DOI: 10.1039/xxxxxxxxxx

Defect driven shapes in nematic droplets: analogies with cell division

Marco Leoni,^{a,b,†,‡} Oksana V. Manyuhina,^{a,†,‡} Mark J. Bowick,^a and M. Cristina Marchetti^a

Received Date

Accepted Date

DOI: 10.1039/xxxxxxxxxx

www.rsc.org/journalname

Building on the striking similarity between the structure of the spindle during mitosis in living cells and nematic textures in confined liquid crystals, we use a continuum model of two-dimensional nematic liquid crystal droplets, to examine the physical aspects of cell division. The model investigates the interplay between bulk elasticity of the microtubule assembly, described as a nematic liquid crystal, and surface elasticity of the cell cortex, modeled as a bounding flexible membrane, in controlling cell shape and division. The centrosomes at the spindle poles correspond to the cores of the topological defects required to accommodate nematic order in a closed geometry. We map out the progression of both healthy bipolar and faulty multi-polar division as a function of an effective parameter that incorporates active processes and controls centrosome separation. A robust prediction, independent of energetic considerations, is that the transition from a single cell to daughters cells occurs at critical value of this parameter. Our model additionally suggests that microtubule anchoring at the cell cortex may play an important role for successful bipolar division. This can be tested experimentally by regulating microtubule anchoring.

†tes Introduction

Living cells have the remarkable ability to divide, generating two daughters from a single mother cell. In eukaryotes this process is termed mitosis¹. A proper division process provides descendants with the correct amount of genetic material needed for subsequent cell growth and development, thus ensuring the continuation of the life cycle. Failure in the division process can lead to malfunctioning daughter cells that may give rise to cancer in multicellular organisms^{2,3}. A key role in mitosis is played by the spindle, a self-organized subcellular structure composed of microtubules that segregates chromosomes during the division process and has been previously described as an active nematic gel. In normal conditions, upon entering mitosis cells possess a single pair of centrosomes⁴ that serve as microtubule nucleating and organizing centers to build the spindle and are driven to opposite sides of the cell during the division process¹. There are some circumstances, however, in which cells may accumulate more than two centrosomes^{2,3,5–7}, perhaps as a result of genetic mutations or previous failed divisions. The precise number and location of

centrosomes determines the organization of the spindle, which can be either bipolar or multipolar. Extra centrosomes have been shown to initiate tumorigenesis in flies⁶ and result in reduced brain development (microcephaly) in mice⁸.

To change shape and generate forces during the various phases of division a cell has to coordinate multiple signals, of both mechanical and chemical origin, on broad time and length scales. To accomplish this task, the cell undergoes a local reorganization of microtubules, which arises spontaneously during the spindle assembly, or can be induced by external constraints, such as micropatterned environments⁹. An assembled spindle usually consists of two poles with microtubule stemming radially from the poles forming two asters (see Fig. 1A). Microtubules extending outwards from the poles are normal to the cell cortex, while in the middle of the spindle the microtubules are aligned tangentially to the cell membrane. The organization, shape, and dynamics of a bipolar spindle are fairly well captured in the framework of active nematic liquid crystals¹⁰, which in the presence of topological defects exhibit spontaneously generated flows induced by active stresses^{11,12} that can drive droplet division¹³. In the final stages of the division process, a key role is also played by the actin cortex, which lies underneath the cell membrane and organizes the acto-myosin contractile ring that pinches apart the two daughter cells^{14–16 17}. The formation of the contractile ring has also been modeled as arising from the

^a Physics Department, Syracuse University, Syracuse, NY 13244, USA.

^b Institut Curie, PSL Research University, CNRS, UMR 168, 26 rue d'Ulm, F-75005, Paris, France.

[†] 'Present address:' mleoni@syr.edu; omanyuhi@syr.edu

[‡] 'These authors contributed equally to this work'

spontaneous organization of an active nematic gel^{14,15}.

Inspired by this previous work, we liken the spindle of a dividing cell to a droplet of nematic liquid crystal bounded by a flexible membrane representing the cell cortex. The structure of the microtubules in the spindle is described by the orientational order of the nematic, with the spindle poles corresponding to the defect structures that are required by topology when confining a nematic droplet. We then model microtubule organization and cell shape changes during division by examining the interplay of bulk and boundary elasticity in controlling the energetics of defect textures as a function of the separation of the spindle poles. Using entirely analytical methods, we show that the nematic droplet evolves from a singly connected structure of evolving shape (a single cell) to two disconnected structures (the two daughter cells) as a function of a single dimensionless parameter that controls spindle pole separation and the associated cell shape.

Of course cell division is an out-of-equilibrium process, with spontaneous organization and shape changes that occur over time and are driven by complex active processes inside the cell. Our model does not explicitly describe nonequilibrium active processes. Instead the active processes that drive cell division are incorporated via a single effective parameter ξ proportional to the spindle poles separation during bipolar division. We assume that the time scales associated with the active rearrangements in the spindle structure are fast compared to those controlling the time evolution of the pole separation, and treat the spindle structure itself as a passive nematic, implicitly incorporating all active processes in the time dependence of $\xi(t)$. Using this minimal effective model, we then evaluate the energy of our “dividing droplet” as a function of cell shape, as tuned by ξ , and controlled by the interplay of the bulk nematic elasticity of the spindle, the bending rigidity and tension of the boundary that models the cell cortex, and the strength of the anchoring of the microtubule nematic to the cell cortex. We show that a critical value of ξ separates singly connected from divided droplets. Importantly, the prediction of this critical value is robust, independent from energetic considerations. Additionally, we propose an energetic criterion for successful division, and use it to construct a phase diagram of cell shapes during the division process.

Our model is two-dimensional and accounts for the interplay of bulk and cortex elasticity. It can describe both healthy (bipolar) cell division, as well as faulty divisions driven by multipolar spindles. Within our model anchoring of microtubules at the droplet boundary is necessary for successful bipolar division, suggesting that a similar scenario may hold for living cells. This prediction could be tested experimentally for example by regulating the expression of proteins – e.g., of the EB family¹⁸ – that control the attachment of microtubules to the cell cortex. It also suggests that the coupling of microtubules to the cell cortex must be incorporated for understanding the mechanics of the division process.

By examining tripolar spindles, we quantify the conditions that control whether the cell divides into three identical daughter cells or into two cells in terms of an angle characterizing the geometry of the triangular arrangements of the three centrosomes. Remarkably, our prediction for this angle is consistent with experimental observations in populations of *Drosophila* cells¹⁹.

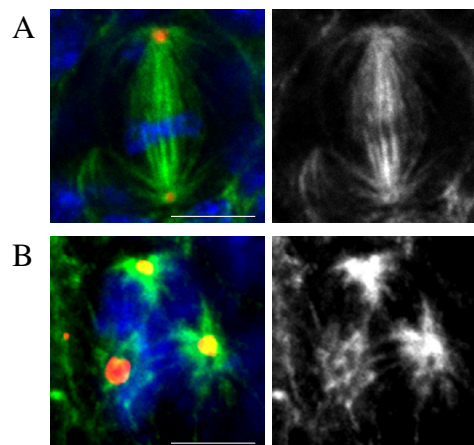


Fig. 1 Images of *Drosophila* third instar larval neural stem cells (neuroblast), labelled with antibodies against tubulin (shown in green) and centrosomes (shown in red). DNA is shown in blue. A: Wild-type neuroblast in metaphase showing a bipolar microtubule array emanating from both centrosomes. B: A mutant neuroblast that contains extra centrosomes forms a tripolar spindle. Image courtesy of Maddalena Nano from the Basto lab, at UMR144 Institut Curie, Paris, France. Scale bar = 7 μm .

2 Model

Inspired by images of cell mitosis like the ones shown in Fig. 1, we explore the analogy between the division of biological cells and the interplay of elasticity and surface anchoring in controlling the shape of nematic liquid crystal droplets. Focusing on the two-dimensional cross-section of a cell, the star-like assembly of microtubules around the nucleus before mitosis resembles the $+1$ defect that is required by topology in a circular nematic droplet with normal anchoring. When the cell starts dividing the microtubule arrangement in the bipolar spindle resembles two $+1$ defects separated by a growing distance, while the cell boundary deforms. To ensure conservation of the topological charge a total -1 charge is then distributed along the cell boundary through variations in the orientation of nematic order relative to the spatially varying normal²⁰. To quantify the analogy between dividing cells and liquid crystal droplets we map the microtubule assembly onto the nematic director field and the centrosomes that drive the spindle organization (displayed as localized red regions in Fig. 1) onto the cores of topological defects in the liquid crystal. We then examine how nematic elasticity competes with the surface anchoring of the microtubules at the deformable cell membrane and the required defects in controlling cell shape and topology. The paradigm proposed below is capable of accounting for both healthy (bipolar) mitosis as displayed in the upper row of Fig. 1, as well as abnormal mitosis, when the spindle can divide in three or more parts, as shown in the bottom row of images of Fig. 1. In the case of three or more centrosomes the splitting of the nuclear content is generally accompanied with an abnormal DNA configuration in a region void of microtubules (the blue areas in Fig. 1). In our model these regions correspond the negative-charge defects, for instance a $-1/2$ disclination at the center of a tripolar spindle.

We restrict ourselves to two-dimensional droplets that could

describe cells of height much smaller than their lateral extent, as is for instance the case for epithelial cells. We ignore (de)polymerization dynamics of microtubules, which occurs on timescales of the order of seconds, and model cell shape changes, which can occur on timescales of hours and are associated with our parameter ξ , as an adiabatic process^{1,21} as outlined in the introduction.

The free energy of our nematic droplet (a.k.a. model cell) is given by

$$F = K \int_{\Sigma} d^2x \underbrace{|\nabla \mathbf{n}|^2}_{\text{elastic}} + \int_{\partial \Sigma} ds \left[\underbrace{k_b (\nabla \cdot \mathbf{v})^2}_{\text{bending}} + \underbrace{\gamma_c}_{\text{tension}} - \underbrace{W_a (\mathbf{n} \cdot \mathbf{v})^2}_{\text{anchoring}} \right]. \quad (1)$$

The first term on the right hand side of (1) describes the cost of elastic deformation of a 2D nematic droplet spanning a domain Σ , with isotropic elastic constant K and unit vector \mathbf{n} characterizing the local orientation of microtubules²². The droplet is bound by a flexible boundary $\partial \Sigma$ of bending rigidity k_b and line tension γ_c describing the cell cortex. Finally, the last term incorporates the strength $W_a > 0$ of the anchoring of the nematic to the boundary, with \mathbf{v} the unit normal pointing towards the outside of the cell.

Assuming a cortex thickness of ~ 100 nm, the membrane properties in (1) can be estimated from experimental measurements as $k_b \propto 10^{-19} \div 10^{-16}$ J; $\gamma_c \propto 5 \cdot 10^{-3}$ J/m²²³. There is, however, no direct information available for K and W_a . Typical values for liquid crystals are $K \simeq 10^{-11}$ J/m and $W_a \propto 10^{-7} - 10^{-3}$ J/m²²², but these values are likely to be quite different in living cells. Below we show how our work can be used to infer a prediction for the value of W_a .

Our goal is to determine the shape of the nematic droplet as a function of the configuration and topology of the enclosed defects by minimizing the free energy, (1), with respect to the angle α , with $\mathbf{n} = \cos \alpha \mathbf{e}_x + \sin \alpha \mathbf{e}_y$. The resulting equations (7), given in the Appendix 4.1, cannot, however, be solved analytically. To proceed we first neglect anchoring and simply minimize the elastic (bulk) part of the nematic free energy with stress-free boundary conditions, which gives

$$\nabla^2 \alpha = 0, \quad [\mathbf{v} \cdot \nabla \alpha]_{\partial \Sigma} = 0, \quad (2)$$

Equations (2) yield a family of solutions for possible cell shapes consistent with a prescribed defect configuration. We will then assume that the physical solution can be identified with the one from this family that minimizes the full free energy, (1), including the anchoring energy. The validity of this approximate method is tested via a perturbative scheme in the Appendix 4.5.

It is convenient to rewrite (2) in the complex plane as

$$\partial_z \partial_{\bar{z}} \alpha = 0, \quad \left[\partial_z \alpha e^{i\varphi} + \partial_{\bar{z}} \alpha e^{-i\varphi} \right]_{\partial \Sigma} = 0, \quad (3)$$

with $z = x + iy$, $\bar{z} = x - iy$ and φ the angle of \mathbf{v} with the x -axis. For a configuration of the director field with defects of strength q_k located at positions z_k , the angle α can then be written in terms of a potential $\Omega(z) = \prod_k (z - z_k)^{q_k}$ as

$$\alpha = [\log \Omega(z) - \log \Omega(\bar{z})] / (2i). \quad (4)$$

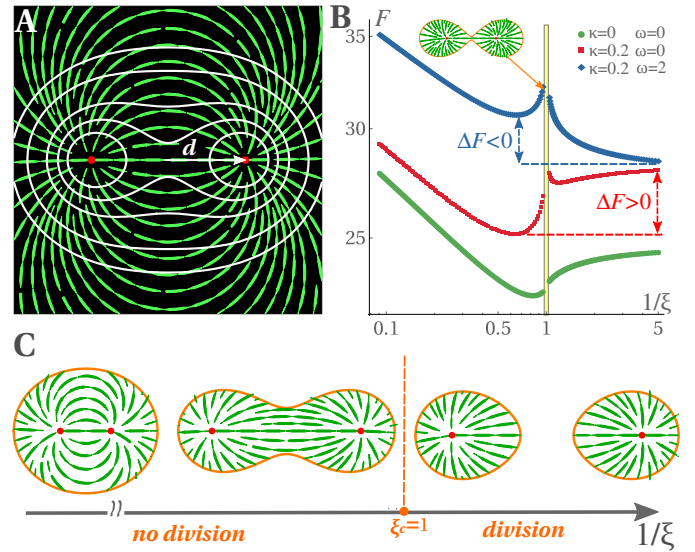


Fig. 2 A. Nematic structure corresponding to two +1 defects separated by a distance d . The green dashed lines describe the direction of the nematic director \mathbf{n} , representing orientation of the microtubule in a bipolar mitotic spindle. The red dots are the cores of the topological defects representing the centrosomes. The solid white lines are the family of boundaries that minimize the energy with stress free boundary conditions ((6)), with constant d . B. The free energy (1) as function of the shape parameter ξ^{-1} , for the defect configuration shown in A, with defect core size $\varepsilon = 0.1R_0$ for various values of κ and ω , with $\gamma = 0$. We define $\Delta F = F_f - F_m$, where F_m is the minimum free energy before division ($\xi^{-1} < 1$) and F_f is the final energy for $\xi^{-1} \gg 1$. The yellow region excludes the singularity at the critical value $\xi_c = 1$ associated with the pinching-off of cells at division and accounts for the finite thickness of the cortex not incorporated in our continuum model. C. Shapes of nematic droplets with constant area: circular ($\xi \gg 1$); peanut ($\xi \simeq 1.2$ minimum of the green curve in B); divided ($\xi < 1$).

For instance, for a single +1 defect at the origin we have $\Omega = z$. In this case the stress-free boundary condition, given by the second of (2), is satisfied by a set of concentric circles of radius R_0 in the complex plane defined by $z\bar{z} = R_0^2$. More generally, the boundary condition requires $\mathcal{F}(\{z_k\}) \equiv [\Omega(z) \cdot \Omega(\bar{z})]_{\partial \Sigma} = \text{constant}$ (see Appendix 4.2 for details) and determines the shape of the boundary $\partial \Sigma$ for a given defect configuration $\Omega(z)$. For symmetric defect configurations, consisting of positive +1 defects at equal distance d from the center of the structure, like the bipolar, tripolar and quadrupolar arrangements shown in Figs. 2, 4, 5, the shape of the boundary $\partial \Sigma$ is determined by the boundary condition that can be written in the form *

$$[\Omega(z/d) \cdot \Omega(\bar{z}/d)]_{\partial \Sigma} = \xi, \quad (5)$$

where ξ is a dimensionless parameter that determines the family of allowed shapes.

In the next section we employ this method to describe the family shapes obtained from (4) and (5) for the case of two +1 defects corresponding to healthy bipolar division and demonstrate

* For the tripolar configuration the left hand side of (5) additionally depends on an angle that characterizes the shape of the triangle.

the role of anchoring energy in shape selection.

2.1 Shapes with two defects: bipolar division

Here we apply the method to describe shape selection for a nematic droplet with a symmetric arrangement of two +1 defects separated by a distance $2d$, as shown in Fig 2, with $\Omega(z) = (z-d)(z+d)$. Using polar coordinates (r, ϑ) , with $z = re^{i\vartheta}$, the family of allowed boundaries obtained from (5) with stress free boundary conditions is given by

$$r_{\pm}(\vartheta) = d\sqrt{\cos(2\vartheta) \pm \sqrt{\xi - \sin^2(2\vartheta)}}. \quad (6)$$

The corresponding curves are shown in Fig. 2A for a range of values of ξ . When $\xi > 1$ the droplet is a simply connected domain defined by r_+ , while for $\xi < 1$ the droplet splits into two smaller domains, outlined by the radius vectors r_{\pm} (see Fig. 2C).

In order to select from this family of equipotential boundaries those that correspond to possible shapes of a cell with two centrosomes we now proceed as follows. First, instead of looking at shapes of varying area for fixed value of the defect separation d , we impose cell incompressibility in $2D$, i.e., require the cell area to be constant and allow the distance d to vary, as shown in Fig. 2C[†]. This amounts to considering d itself to be an increasing function of ξ (see for details Appendix 4.3, (16) and (17)), with the shapes becoming more elongated with increasing d . This amounts to assuming that the parameter ξ incorporates all active processes that drive cell division and sets the centrosome separation $2d(\xi)$. Secondly, we incorporate boundary tension and bending as well as anchoring by calculating the full free energy as given in (1) for a given cell shape and using the behavior of the energy to define a criterion for identifying preferred cell shapes.

Measuring lengths in units of the typical size $R_0 \sim 10 \mu\text{m}$ of the cell and energies in units of the nematic stiffness K , the free energy depends on three dimensionless parameters: the scaled bending rigidity $\kappa = k_b/(KR_0)$ and tension $\gamma = \gamma_c R_0/K$ of the cell boundary, and $\omega = W_a R_0/K$ that measures the relative strength of anchoring and nematic elasticity. The full free energy given in (1) corresponding to a cell configuration $d(\xi)$ is shown in Fig 2B as a function of ξ for a few parameter values. For $\xi^{-1} \ll 1$ the cell is almost round, just before entering the anaphase¹. The free energy has a local minimum F_m for $\xi^{-1} < 1$ and it diverges at $\xi = 1$. This divergence is nonphysical and is cutoff by the finite thickness of the droplet boundary (cell membrane) that has been neglected in our model. This is indicated by the yellow vertical boundaries in Fig. 2B. Based on the analogy between cells and nematic droplets outlined above, we conjecture that local minimum of the free energy for $\xi^{-1} < 1$ corresponds to the most stable cell shapes at the end of anaphase where the two centrosomes are already well separated, and that the energy barrier at $\xi = \xi_c = 1$ represents the energy needed to break the quasi-pinned droplet into two pieces. In living cells this energy can be provided at

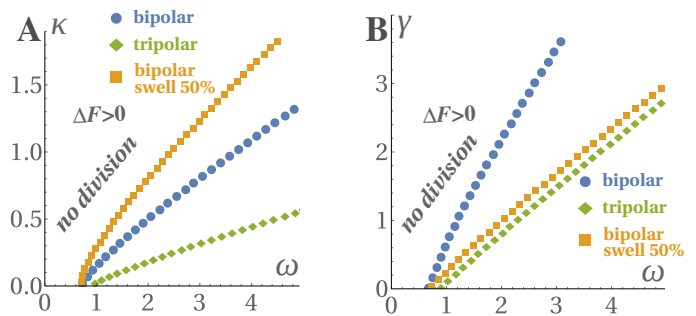


Fig. 3 Phase diagrams for a nematic droplet with bipolar (blue dots) and symmetric tripolar (green diamonds, with $\beta = \pi/3$, see next section) division assuming constant surface area enclosed by the droplet for $\gamma = 0$ (A) and $\kappa = 0$ (B). Droplet division (according to our criterion, $\Delta F < 0$) occurs in the region between the curves and the ω axis and requires a finite value of anchoring $\omega \neq 0$ at the cell boundary. The orange squares represent the division boundary obtained when swelling of both daughter droplets and centrosome area by 50% is included.

the onset of cytokinesis by the cytokinetic ring, which effectively acts as a rope pulled by active forces, generating a constriction at the cell midpoint^{14,15}. We further conjecture that a successful division is governed by the sign of $\Delta F = F_f - F_m < 0$, where $F_f = F(1/\xi \rightarrow \infty)$ is the final free energy for $\xi^{-1} \gg 1$, and that cell division will occur only if $\Delta F < 0$. This condition is satisfied, for instance, for the parameter values corresponding to the blue curve of Fig. 2B, but not for the other two, where $\Delta F > 0$.

Using this criterion, we have constructed phase diagrams displayed in Fig. 3 identifying the regions of parameters corresponding to successful cell division. The region where division occurs is enclosed between the line and the ω -axis. Remarkably, we find that in all cases, anchoring of filaments to the cell boundary, $\omega \sim O(1)$, is necessary for division.

Using experimental values of k_b and γ_c , our model can be used to infer the value of the anchoring strength W_a in two ways. First, when line tension is negligible ($\gamma \ll 1$) cell division occurs for values of ω such that $\omega \sim \kappa$ (blue dots in Fig. 3A), corresponding to $W_a \sim k_b/R_0^2$. For $R_0 \sim 10 \mu\text{m}$, we would then estimate $W_a \sim 10^{-9} \div 10^{-6} \text{ J/m}^2$. Secondly, in the opposite limit $\gamma \gg \kappa$ (expected e.g. for large round cells $R_0 > \sqrt{\kappa_b/\gamma_c}$), cell division occurs for values of $\omega \sim \gamma$, corresponding to $W_a \sim \gamma_c \sim 5 \cdot 10^{-3} \text{ J/m}^2$. This value, significantly higher than the previous estimate, is closer to conventional values for liquid crystals²². In spite of the ambiguity in the estimate of the anchoring strength, an important prediction of our model is that in all cases the anchoring of filaments to the cell cortex is necessary for a successful bipolar cell division.

There is experimental evidence that mammalian cells swell prior to cell division²⁴ and that centrosomes may also change size²⁵. Additionally, a correlation between cell and centrosome sizes has been demonstrated in *C. Elegans*²⁶. Inspired by these findings, we have examined the influence of cell and centrosome sizes on the energetics of our model. The size of the centrosomes corresponds to the core size ε of topological defects and enters as a small-scale cutoff in the calculation of the elastic energy. The effect of a simultaneous 50% swelling of both cell and centrosomes prior to division is shown in Fig. 3A,B (orange squares).

[†] Cells are generally treated as incompressible in $3D$. Our model is strictly two-dimensional and represents a $2D$ analogue where the cell is treated as a $2D$ object and height fluctuations are neglected.

We find that when $\gamma = 0$ (frame A of Fig. 3) swelling facilitates division even at large bending rigidity, while when $\kappa = 0$ swelling suppresses division, with the suppression increasing with line tension. In other words, our model suggests that cells can divide more easily when the boundary tension is small and the cell can swell easily. Conversely, this suggests that those cells where division is preceded by swelling are characterized by small values of boundary tension, while the dominant contribution to the deformation energy comes from bending elasticity of the cell cortex, indicating that $W_a \sim 10^{-9} \div 10^{-6}$ J/m² may be the more plausible estimate.

Finally, we have verified that when varied separately, neither the centrosome size, ε , nor the cell size significantly impact cell division.

2.2 Multipolar division

Cells are sometimes observed to divide abnormally into more than two daughter cells (multipolar cell division). This can be a consequence of genetic modifications, controlling the expression levels of proteins that are important for mitosis, or of the failure of a previous cell division. What drives such faulty divisions is not understood, although accumulation of extra centrosomes has been suggested as a possible cause^{2,3,7}. Our model allows us to analyze configurations of microtubules corresponding to multipolar spindles by modeling them as nematic droplets with more complex defect structures, consisting of both positively charged defects representing centrosomes and negatively charged defects representing abnormal DNA configurations which could be due to abnormal DNA content^{7,27}, shown as red and blue dots, respectively, in Figs. 4 and 5. Combining positive and negative strength defects one can design defect textures that closely resembles the configuration of microtubules inside cells with either tripolar^{7,19}, Fig. 1B, or quadrupolar^{7,27} spindles. The size and orientation of symmetric tripolar and quadrupolar defect configurations can be characterized by the distance d from the center of each of the $+1$ disclinations and by their angular separation β , as shown in Figs. 4C, 5C. The negative $-1/2$ disclination in the case of tripolar spindle (Fig. 4A,B) and the -1 defect for the quadrupolar spindle (Fig. 5A) account for the absence of nematic order at the center of the droplet, or abnormal DNA configurations at the center of these faulty dividing cells. This interpretation is also supported by other experimental works²⁸ showing that the DNA can act as a nucleator of microtubules and can affect multipolar spindle organization.

In a tripolar spindle, two distinct pathways of cell division arise for small values of the centrosome angular separation $\beta < \pi/3$. A tripolar droplet with a hole in the nematic texture at its center can either split into two domains with unequal number of centrosomes or into three equal domains as illustrated in Fig. 4C. When $\beta \geq \pi/3$ the only possible transition is from one into three cells (see Fig. 4C). Similarly, the division of a quadrupolar droplet can also follow two pathways, as illustrated in Fig. 5C. We conjecture again that the selection of one of the two possible pathways is controlled by energetics according to the same rules we introduced for the bipolar case. For symmetric multipolar spindles cell

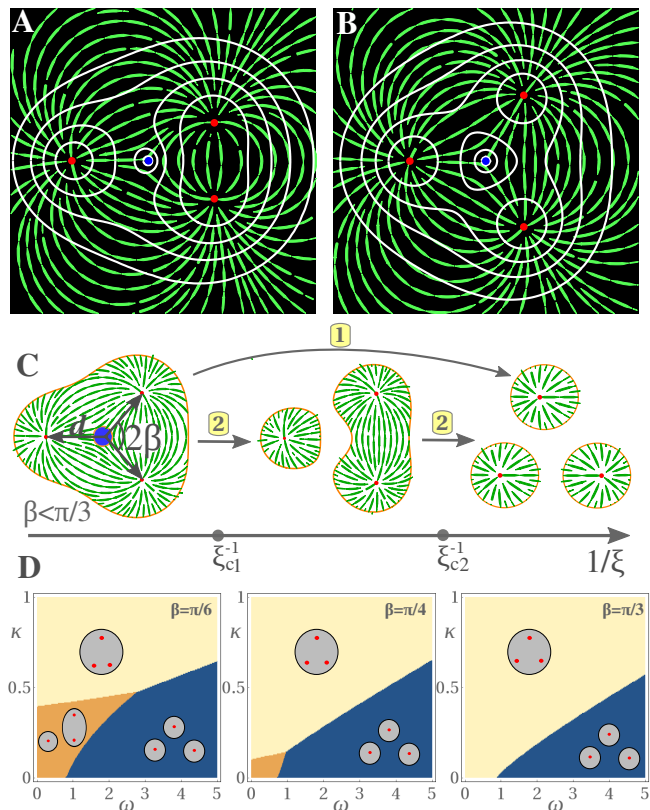


Fig. 4 Nematic defect textures and associated equi-energy boundaries for tripolar droplets with three $+1$ defects, at distance d from the center, separated by an angle β for $\beta = \pi/6$ (A) and $\beta = \pi/3$ (B). The color-code is the same as in Fig. 2. Additionally, the blue dots are $-1/2$ disclinations of the director field, representing abnormal DNA configurations. C. Division can occur following two distinct pathways: 1) a direct division into three daughter droplets; or 2) a two-step division of one cell into three daughter droplets via an intermediate structure of bipolar droplets with distinct numbers of defects. D. Phase diagrams showing regions when the division into three (blue color) or two (orange) daughter cells is energetically favored for different initial configurations of centrosomes with opening angle 2β . Bipolar division occurs for $\beta \lesssim \pi/4$, in good agreement with experiments on *Drosophila* wing disc epithelium¹⁹, and for small values of anchoring ω . The values of the remaining parameters are $\gamma = 0$ and $\varepsilon = 0.01$.

shapes depend at least on two parameters, ξ and the angle β defined in Figs. 4C, 5C. There are two critical lines $\xi_{c1}(\beta)$ and $\xi_{c2}(\beta)$ that control the transitions from single connected domains to two daughter cells and from two to three or four cells, respectively, as shown in Figs. 4C, 5C and summarized in Fig. 6 in Appendix.

As discussed above, the line tension γ does not play an important role in the energetics, thus it will be neglected for tripolar spindles. The regions of stability of dividing tripolar spindles are shown in Fig. 4D. Note that a small value of β promotes cell division, and specifically promotes fission into two or three daughter cells. An important difference as compared to the case of bipolar spindles (see Fig. 3), is that here for small angles β , division can occur also in the absence of anchoring, $\omega = 0$. This suggests that in multipolar spindles cells may regulate the strength of ω depending on the angular separation β to ensure the division process. Finally, for $\beta \gtrsim \pi/4$ the division of the tripolar spindle into

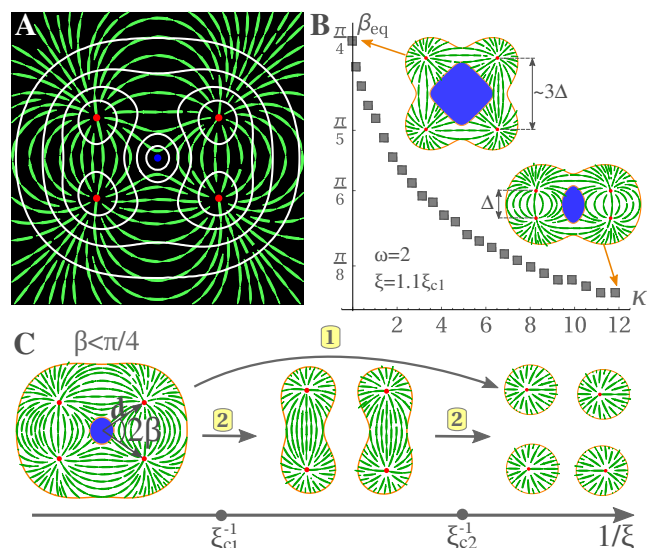


Fig. 5 A. Nematic defect textures and associated equi-energy boundaries for quadrupolar droplets with four $+1$ defects, at distance d from the center and separated by angle β , and a -1 disclination, representing abnormal DNA configurations, at the center. The color-code is as in Fig. 2. B. The angle β_{eq} that minimizes the free energy (1) before division for the symmetric quadrupolar configuration as a function of the rescaled bending rigidity, κ . β_{eq} decreases with increasing κ , resembling centrosome clustering⁵. Studying this phenomenon may elucidate the physical mechanisms governing clustering in multipolar spindles. C. Division can occur following two distinct pathways: 1) directly into four identical cells; or 2) indirectly into four daughter droplets, through an intermediate state of two bipolar droplets with equal numbers of defects.

two daughter cells is strongly suppressed as compared to division in three cells, and does not occur for $\beta \geq \pi/3$. This result is in agreement with the experimental observation of cell division in populations of *Drosophila* epithelial cells *in vivo*, including quantitative agreement for the value of the initial angle β suppressing dipolar division¹⁹.

3 Discussion and concluding remarks

Growth and division are the hallmark of living systems, but related processes are observed also in inert matter. For instance, atomic nuclei can grow by capturing neutrons²⁹ and then divide into two lighter daughter nuclei via a fission process that releases energy and has been modeled using an analogy with liquid droplets³⁰. In living cells division is driven by active processes that underlie the assembly and reorganization of the spindle, a microtubule structure that resembles a tactoid – an elongated nematic liquid crystal droplet with two sharp poles, with shape being mainly controlled surface tension anisotropy (strong tangential anchoring)^{31,32}. Inspired by these ideas, we have studied two-dimensional nematic droplets bound by a membrane with finite bending rigidity and line tension to gain insight on the interplay between spindle elasticity and the properties of the bounding cell cortex in dividing cells. While the importance of nematic alignment of microtubules in controlling the organization of the spindle has been demonstrated before¹⁰, new elements of our model are the proposed connection between centrosomes and the

defects that are required by topology in nematic liquid crystals and their role in controlling shape changes. Thanks to this powerful analogy, we investigate analytically the interplay of bulk and surface elasticity, including the role of anchoring of microtubules to the cell boundary, in controlling cell shape. Our model applies provided the cell cortical boundary is deformable and there is a strong coupling between its shape and microtubule organization, as may be the case for epithelial animal cells. It does not, however, apply to plant cells that have rigid cell-walls whereby cells grow thanks to the help of turgor pressure³³.

Our suggestion that cell division is driven entirely by the direct mechanical deformations that the spindle induces on the cortex appears in contrast with the accepted view that the spindle initiates signaling pathways that control the localization and activity of different molecules on the cortex, which in turn cause the shape changes associated with cell division^{34–37}. It should be stressed, however, that our work describes a coarse-grained model where biochemical signaling processes, although not explicitly included, should be thought of as determining the effective parameters of the model, such as the shape parameter ξ that controls the separation of the spindle's poles and the parameters κ , γ and ω controlling the mechanical properties of the cortex and the strength of anchoring. Our work could therefore be reconciled with the current literature for instance by assuming that the cortex properties κ , γ and ω depend on the shape parameter ξ , or are more generally time-dependent and varying along the cortex contour to mimic how spindle initiates signaling pathways.

Our work makes several predictions that emphasize the key role of centrosomes in driving both healthy bipolar and faulty multipolar division processes. The first important new result is that anchoring is always required for successful bipolar cell division. This prediction could be tested experimentally by regulating the level of expression of proteins (e.g., of the EB family) responsible for connecting microtubules to the cell cortex. Alternatively, one may control the anchoring by mechanically intervening on such connections, for instance with laser ablation³⁸. Our theory also provides an estimate of the anchoring strength as $W_a \sim 10^{-9} \div 10^{-6}$ J/m², lower than typical values for liquid crystals. Our second prediction concerns the role of the boundary elasticity in controlling the fate of cell division, captured in our continuum model by two parameters: the bending rigidity κ and the tension γ . The bending rigidity κ of the cortical boundary could be modulated by varying acto-myosin activity for instance via the addition of commercially available drugs such as blebbistatin. The boundary tension γ may perhaps be varied by acting on the physical properties of the culture medium surrounding the cells (e.g., its viscosity). Experiments of this type would provide a direct connection between the continuum mechanics of cells and various subcellular signaling processes. Thirdly, for tripolar spindles, we find that there is a critical angle characterizing centrosome organisation beyond which division into three daughter cells is more likely than bipolar division. Remarkably, a similar phenomenon was observed in *Drosophila* epithelial cells¹⁹. The critical angle predicted by our theory is in good agreement with the experimental measurements. Finally, we have demonstrated that the combined effect of cell and centrosome size change (swelling)

can help division, allowing it to occur in regions of the parameter space which are inaccessible in the absence of swelling.

Many open questions lie ahead. An important challenge is to relate the shape parameter ξ to active processes in the cell. This will require starting from a more microscopic model that incorporates dynamical processes such as microtubule polymerization and depolymerization as well as the motor's binding/unbinding and then obtain mesoscopic equations via coarse-graining procedures. This is a challenging open problem that remains beyond the scope of the present work. It would also be interesting to extend the model to 3D, which may be relevant for other types of cells, e.g., sea urchins²⁷. Our model could also be adapted to investigate centrosome clustering⁵. Our preliminary analysis (see Fig. 5B) suggests that bending rigidity κ and surface tension γ can play an important role in controlling the angular separation among defects, hence their clustering. A comprehensive analysis of defect clustering, when the defect separation becomes comparable to their core size, requires a more detailed description of the core region²² and is beyond the scope of the present work. Finally, our results also apply to synthetic active nematic droplets and reconstituted in-vitro systems where orientational order, anchoring of filaments to the boundaries, and boundary elasticity may be designed and tuned more easily than in biological cells.

4 Appendix

4.1 Variational problem: boundary condition

We consider a nematic liquid crystals described by the director $\mathbf{n} = \cos \alpha \mathbf{e}_x + \sin \alpha \mathbf{e}_y$ confined to a domain Σ in 2D, and enclosed by the boundary $\partial\Sigma$ with normal \mathbf{v} , with free energy given by (1). The equilibrium configuration of \mathbf{n} and the associated boundary condition can be found by setting to zero the first variation of the free energy (1) with respect to the angle α , yielding²⁰

$$\nabla^2 \alpha = 0, \quad [K \mathbf{v} \cdot \nabla \alpha + W_a \sin(\alpha - \varphi) \cos(\alpha - \varphi)]_{\partial\Sigma} = 0, \quad (7)$$

where φ is the angle of \mathbf{v} with the x -axis. In order to proceed with analytical methods, we first neglect the anchoring term, so that (7) becomes

$$\nabla^2 \alpha = 0, \quad \mathbf{v} \cdot \nabla \alpha|_{\partial\Sigma} = 0, \quad (8)$$

which corresponds to stress free boundary condition³⁹. The solution of (8) will yield a family of cell shapes. The physical solution will then be selected as the one that minimizes the free energy (1), including the anchoring energy.

It is convenient to work with complex coordinates where (8) becomes

$$\partial_z \partial_{\bar{z}} \alpha = 0, \quad \left[\partial_z \alpha e^{i\varphi} + \partial_{\bar{z}} \alpha e^{-i\varphi} \right]_{\partial\Sigma} = 0, \quad (9)$$

with $z = x + iy$ and $\bar{z} = x - iy$. The general solution α can then be written in terms of the potential $\Omega(z) = \Pi_k(z - z_k)^{q_k}$ as (see (4) in the main text)

$$\alpha = \frac{\log \Omega(z) - \log \Omega(\bar{z})}{2i}, \quad (10)$$

which describes configurations of the director field with defects of strength q_k located at position z_k , where the nematic order vanishes. Here q_k is the winding number of the director around

any closed contour surrounding the defect

$$q_i = \frac{1}{2\pi} \oint ds (\mathbf{n} \times \partial_s \mathbf{n}) = \frac{1}{2\pi} \oint d\alpha. \quad (11)$$

4.2 Solution for cell boundaries

Given the bulk solution for α given by (10), we extend it up to the boundary $\partial\Sigma$ described by a unit normal \mathbf{v} that satisfies the boundary condition $\mathbf{v} \cdot \nabla \alpha|_{\partial\Sigma} = 0$ as follows. First, we parametrize the boundary $\partial\Sigma$ via a curvilinear coordinate s and write $\mathbf{v} = \cos \varphi(s) \mathbf{e}_x + \sin \varphi(s) \mathbf{e}_y$. Next, we assume that the boundary can be parametrized in the complex plane by a Schwarz function $\bar{z} \equiv g(z)$, obtained by solving $f(\frac{z+\bar{z}}{2}, \frac{z-\bar{z}}{2i}) = 0$ for \bar{z} . This can be related to the angle φ as (see e.g.^{40,41})

$$\frac{d\bar{z}}{ds} = g' \frac{dz}{ds} = -ie^{-i\varphi}, \quad \rightarrow \quad \frac{d\bar{z}}{dz} = g' = -e^{-2i\varphi}. \quad (12)$$

Substituting the angle α (10) into (9) and making use of (12), the stress free boundary condition (7) corresponding to $W_a \rightarrow 0$, becomes

$$g' = \frac{\partial_z \alpha}{\partial_{\bar{z}} \alpha} \quad \rightarrow \quad - \left[\frac{\partial_z \Omega(z)}{\Omega(z)} \cdot \frac{\Omega(\bar{z})}{\partial_{\bar{z}} \Omega(\bar{z})} \right]_{\partial\Sigma} = \frac{d\bar{z}}{dz} \Big|_{\partial\Sigma}, \quad (13)$$

or

$$[\log(\Omega(z)) + \log(\Omega(\bar{z}))]_{\partial\Sigma} = \text{const.} \quad (14)$$

It follows from (14) that the function $\mathcal{F}(z, \bar{z}; \{z_k\}) = \Omega(z)\Omega(\bar{z})$ is constant on the boundary. It is then convenient to parametrize the family of allowed shapes corresponding to a given defect configuration in terms of a dimensionless parameter ξ (level set) setting

$$\left[\mathcal{F} \left(\frac{z}{d}, \frac{\bar{z}}{d}; \left\{ \frac{z_k}{d} \right\} \right) \right]_{\partial\Sigma} = \xi, \quad (15)$$

where d measures the distance of the defects from the center of the symmetric defect configuration. More precisely, for bipolar spindles, where $z_k = \pm d$ (Fig. 2A), $2d$ is the separation of the two $+1$ defects. For tripolar and quadrupolar spindles, with $z_k = \{0, -d, de^{\pm i\beta}\}$ (tripolar, Fig. 4A,B) and $z_k = \{0, de^{\pm i\beta}, de^{i(\pi \pm \beta)}\}$ (quadrupolar, Fig. 5A), an additional angle β is needed to describe the defect configuration. Note that the resulting shapes (15) are smooth functions for all values of ξ , except for the critical values ξ_c where the pinching-off of the cell into daughter cells occurs. This is the result of the chosen boundary condition (8), which depends on $\nabla \alpha$. In the opposite limit, when the line tension anisotropy (anchoring) is the dominant term in (7), one would expect to find shapes with cusps, also known in the liquid crystal literature as tactoids³¹. In this limit tactoid-type shapes with cusps and the director field tangential everywhere to the boundary can be obtained either solving for the Schwarz function g as above or using the Wulff construction as in^{32,42}. Interfacial cusp formation, followed by the nucleation of two $+1/2$ disclinations, was found within the Landau-deGennes theory during isotropic-nematic phase transition with homeotropic anchoring at the interface⁴³.

4.3 Incompressibility condition

Eq. (15) parametrizes the family of boundaries shown as white contours in Figs. 2A, 4A-B, 5A, for a given value of d . To compute the actual droplet shapes (see Figs. 2C, 4C, 5C), we assume that the droplet is incompressible, i.e., that its area is constant. In the case of bipolar division the areas before ($\xi > 1$) and after ($\xi < 1$) division, are given respectively, by

$$S_1 = \int_{-\pi}^{\pi} d\vartheta \int_0^{r_1} dr r = d^2 \left[\sqrt{\xi-1} \mathcal{E} \left(\frac{1}{1-\xi} \right) + \sqrt{\xi} \mathcal{E} \left(\frac{1}{\xi} \right) \right], \quad (16)$$

$$S_2 = 2 \int_{-\vartheta_m}^{\vartheta_m} d\vartheta \int_{r_2}^{r_1} dr r = 2d^2 \sqrt{\xi} \mathcal{E} \left(\arcsin \sqrt{\xi} \left| \frac{1}{\xi} \right. \right), \quad (17)$$

where \mathcal{E} is the complete elliptic integral of the second kind. Assuming that $S_1 = \pi R_0^2 = S_2$, the distance d between two defects in (6) becomes a function of ξ . Thus in the two regions, before and after division, d can be expressed as two distinct functions of ξ which match at $\xi_c = 1$.

4.4 Topological transformations

Here we discuss how ξ controls the change of topology that accompanies cell division.

For a tripolar spindle, described as three +1 disclinations surrounding a single -1/2 disclination, the equation for the boundary (15) can be written in polar coordinates as

$$(r^2 + d^2 + 2rd \cos \vartheta)(r^2 + d^2 - 2rd \cos(\vartheta - \beta)) \times \\ \times (r^2 + d^2 - 2rd \cos(\vartheta + \beta)) = \xi r d^5. \quad (18)$$

Unlike (6) for the bipolar case, there is no closed form solution for the radius vector. Using *Mathematica* we can express implicitly $r(d, \xi, \beta, \vartheta)$ and analyze a variety of contours for different angles β and level sets ξ . More important, we identify the extrema of the function (18) and the critical values ξ_{c1} and ξ_{c2} where the topological transitions occur (Fig. 6A) at $\vartheta = 0$, $\vartheta|_{\beta < \pi/3} = \arccos[-\sqrt{(2\cos\beta - \cos(2\beta))/6}]$, $\vartheta|_{\beta > \pi/3} = \arccos[(\cos\beta - 2)/3]$.

For a quadrupolar spindle, described as an arrangement of four +1 disclinations surrounding a -1 disclination, the equation for the boundary (15) can be written in polar coordinates as

$$2r^4 d^4 \cos(4\beta) + 2r^4 d^4 \cos(4\vartheta) + \\ + (r^4 + d^4)(r^4 - 4r^2 d^2 \cos(2\beta) \cos(2\vartheta) + d^4) = \xi r^2 d^6. \quad (19)$$

The critical values of ξ when a single domain splits into two and four domains (Fig. 6B) at $\vartheta = \{0, \pi/2\}$ are

$$\xi_{c1,c2} = \frac{4}{27} \left[\pm 33 \cos(2\beta) \mp \cos(6\beta) + \sqrt{2(7 + \cos(4\beta))^{3/2}} \right]. \quad (20)$$

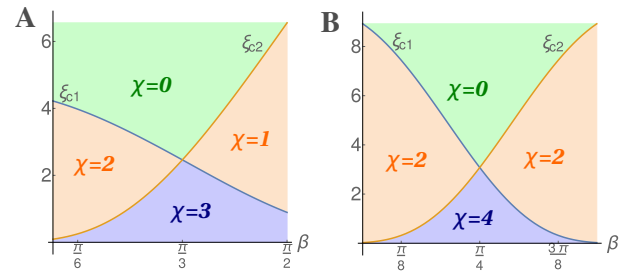


Fig. 6 The regions relating the discrete Euler characteristic χ , with the continuous variation of the parameter ξ in case of tripolar (A) and quadrupolar (B) division. The angle β describes the chosen configuration of +1 defects, with symmetry of the curves (20) around $\beta = \pi/4$ (B).

There is a mathematical relation between the sum of the charges (11) of the defects in the nematic texture, the Euler characteristic χ ⁴⁴ of the confining boundary and the integral of the angle deficit between the director \mathbf{n} and the normal \mathbf{v} along the boundary $\partial\Sigma$, given by²⁰

$$\sum_i q_i - \frac{1}{2\pi} \int_{\partial\Sigma} d(\alpha - \varphi) = \chi, \quad \mathbf{n} \cdot \mathbf{v} = \cos(\alpha - \varphi). \quad (21)$$

In 2D χ is related to the number \mathcal{H} of holes in the nematic texture via $\chi = 1 - \mathcal{H}$. Then for a disc $\chi = 1$ and $\chi = 0$ for an annulus. The Euler characteristic χ can therefore be interpreted as identifying the number of daughter cells after division. Moreover, the director field is on average aligned along the normal to the boundary $\partial\Sigma$, for daughter cells with only one +1 disclination (Fig. 6A-D), as imposed by the conservation law (21). In other cases, considered above where $\sum_i q_i > 1$, the director \mathbf{n} and the normal \mathbf{v} are not aligned, resulting into a non-zero contribution to the integral at the left hand side of the (21). We have shown above that such misalignment is important for triggering cell division.

4.5 Method for obtaining the solution of the boundary condition including anchoring, Eq. (7)

In the preceeding section and in the main text we computed the exact solution, for the shape of the boundary using the simplified boundary condition (8), which corresponds to the limit of vanishingly small anchoring, $W_a \rightarrow 0$. On the other hand, we have shown that the selection of the equilibrium shape itself depends on the value of W_a . In this subsection we present a method to study systematically the effect of the boundary condition corresponding to a finite value of the anchoring parameter W_a on the shape of the boundary, in agreement with previous work⁴⁵. This provides a test of the consistency of the approximate scheme used in the main text. To this end we first rewrite the boundary condition (7) in the complex plane as

$$e^{i\varphi} \partial_z \alpha + e^{-i\varphi} \partial_{\bar{z}} \alpha + \varpi \frac{e^{-2i\varphi} e^{2i\alpha} - e^{2i\varphi} e^{-2i\alpha}}{2i} = 0, \quad (22)$$

where the complex coordinates z, \bar{z} are scaled by the distance $d^{\frac{1}{2}}$ and we have introduced the dimensionless parameter $\varpi \equiv W_a d / 2K$. We can then solve (22) for small ϖ by expanding the Schwarz function g (12) as a power series in ϖ ,

$$g = g_0 + \varpi g_1 + \varpi^2 g_2 \dots \quad (23)$$

For simplicity, let us consider the case of bipolar division, with $\alpha = \text{Im} \log(z^2 - d^2)$. Substituting (23) into (22) and including terms up to first order in ϖ , we solve to each order, with the result

$$O(\varpi^0): \quad g_0 = d \sqrt{1 + \frac{\xi}{(z/d)^2 - 1}}, \quad (24)$$

$$O(\varpi^1): \quad g_1' = \left(\frac{e^{2i\alpha} g_0'}{2i} - \frac{e^{-2i\alpha}}{2ig_0'} \right) \frac{g_0'}{\partial_z \alpha \sqrt{-g_0'} - \partial_{\bar{z}} \alpha / \sqrt{-g_0'}}. \quad (25)$$

The zero-th order solution, g_0 , is the solution of Eq. (13) and is the same solution plotted in Fig. 2 and expressed in polar coordinates in Eq. (6) of the main text. The correction g_1 accounts for the leading order effect of anchoring on modifying the shape of the solution. To obtain an explicit expression for g_1 we write it as a power series, around the position of the defect core at $z = d$, as

$$g_1 = \sum_{i=0}^{\infty} a_i \left(\frac{z}{d} - 1 \right)^{\frac{2i-1}{4}}. \quad (26)$$

The coefficients a_i of the power series are fixed by matching term by term the left-hand-side and the right-hand-side of the Eq. (25), using the known form of g_0 . This yields

$$a_0 = -\frac{\xi^{3/4}}{2^{1/4}}, \quad a_1 = 0, \quad a_2 = \frac{3\xi - 4}{8(2\xi)^{1/4}}, \quad a_3 = -\frac{\xi^{1/4}}{5 \cdot 2^{3/4}}, \quad (27)$$

$$a_4 = \frac{336 - \xi(312 + 11\xi)}{896 \cdot (2\xi^5)^{1/4}}, \quad a_5 = \frac{4 - 7\xi}{72(2\xi)^{3/4}}, \quad \dots \quad (28)$$

In Fig. 7 we compare the contour $\bar{z} = g_0$ and the contours $\bar{z} = g_0 + \varpi g_1$, obtained following this procedure, including the first two (red) and six (green) terms in the power series (26). We have verified that including higher order terms in the expansion of g_1 does not further change the shape of the green curve, suggesting that the power series (26) converges. Moreover, the resulting shapes with finite anchoring, $\varpi = 0.4$, closely resemble the shapes computed in the main text with the simplified boundary condition (no anchoring). We conclude that the approach proposed here and summarized in Fig. 7 is consistent with the results presented in the main text showing that anchoring is not relevant in determining the shapes but it plays a key role in controlling the selection of the shape according to our energetic criterion.

Acknowledgements

M. L. acknowledges financial support by the ICAM Branch Contri-

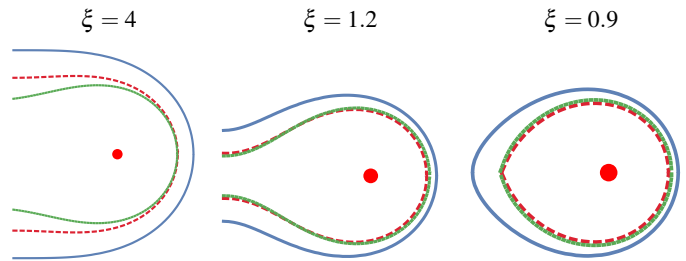


Fig. 7 Comparison of the boundary contours obtained via various approximations: without anchoring, as in the main text, (blue curve, $\bar{z} = g_0$) and with $\varpi = 0.4$ (red and green curves, $\bar{z} = g_0 + \varpi g_1$). We show the solution of (22) only around the +1 disclination, since the solutions have mirror symmetry with respect to the vertical axis, so that blue curves here coincide with the right portions of the contours shown in Fig. 2. The three panels are for $\xi = 4$, $\xi = 1.2$ and $\xi = 0.9$, as indicated. The correction g_1 due to anchoring is evaluated including terms up to $i = 2$ (red curve) and $i = 6$ (green curve) in Eq. (26).

butions and stimulating discussions with Maddalena Nano. MCM was supported by the Simons Foundation through a Targeted Grant in the Mathematical Modeling of Living Systems, award No. 342354, and by the National Science Foundation through awards DMR-1305184 and DMR-1609208. All authors acknowledge support from the Syracuse University Soft Matter Program.

References

- 1 B. Albert *et al.*, *The Molecular Biology of the Cell*, 4th ed., Garland Science, 2002.
- 2 B. R. Brinkley and T. M. Goepfert, *Cell Mot. and the Cytoskeleton*, 1998, **41**, 281–288.
- 3 S. A. Godinho and D. Pellman, *Phil. Trans. R. Soc. B*, 2014, **369**, 20130467.
- 4 T. Stearns, *Science*, 2015, **1091**, 348.
- 5 V. Marthiens, M. Piel and R. Basto, *J Cell Sci*, 2012, **125**, 3281–3292.
- 6 R. Basto, K. Brunk, T. Vinadogrova, N. Peel, A. Franz, A. Khodjakov and J. Raff, *Cell*, 2008, **133**, 1032–1042.
- 7 A. W. Duncan, M. H. Taylor, R. D. Hickey, A. E. H. Newell, M. L. Lenzi, S. B. Olson, M. J. Finegold and M. Grompe, *Nature*, 2010, **467**, 707.
- 8 V. Marthiens, M. A. Rujano, C. Pennetier, S. Tessier, P. Paul-Gilloteaux and R. Basto, *Nat. Cell Biol.*, 2013, **15**, 731.
- 9 M. Théry, A. Jiménez-Dalmaroni, V. Racine, M. Bornens and F. Jülicher, *Nature*, 2007, **447**, 493–496.
- 10 J. Brugués and D. Needleman, *Proc. Natl. Acad. Sci. USA*, 2014, **111**, 18496–18500.
- 11 T. Sanchez, D. T. N. Chen, S. J. DeCamp, M. Heymann and Z. Dogic, *Nature*, 2012, **491**, 431–435.
- 12 L. Giomi, M. J. Bowick, X. Ma and M. C. Marchetti, *Phys. Rev. Lett.*, 2013, **110**, 228101.
- 13 L. Giomi and A. DeSimone, *Phys. Rev. Lett.*, 2014, **112**, 147802.
- 14 G. Salbreux, J. Prost and J. F. Joanny, *Phys. Rev. Lett.*, 2009, **103**, 058102.
- 15 H. Turlier, B. Audoly, J. Prost and J. F. Joanny, *Biophys. J.*,

[‡] Alternatively one could use the typical size of the domain R_0 . Here these two sizes are related through the incompressibility condition of the domain, $d(R_0)$.

- 2014, **106**, 114–123.
- 16 J. Sedzinski, M. Biro, A. Oswald, J. Tinevez, G. Salbreux and E. Paluch, *Nature*, 2011, **476**, 462–466.
- 17 J. A. Åström, S. von Althaus, P. B. S. Kumarb and M. Karttunen, *Soft Matter*, 2010, **6**, 5375.
- 18 J. S. Tirnauer and B. E. Bierer, *J. Cell Biol.*, 2000, **149**, 761–766.
- 19 D. Sabino, D. Gogendeau, D. Gambarotto, M. Nano, C. Penetier, F. Dingli, G. Arras, D. Loew and R. Basto, *Curr. Biol.*, 2015, **25**, 879–889.
- 20 O. V. Manyuhina, K. B. Lawlor, M. C. Marchetti and M. J. Bowick, *Soft Matter*, 2015, **11**, 6099.
- 21 A. Desai and T. J. Mitchison, *Annu. Rev. Cell Dev. Biol.*, 1997, **13**, 83–117.
- 22 P. G. DeGennes and J. Prost, *The Physics of Liquid Crystals*, 2nd ed., Oxford University Press, 1993.
- 23 R. Alert, J. Casademunt, J. Brugués and P. Sens, *Biophys. J.*, 2015, **108**, 1878–86.
- 24 E. Zlotek-Zlotkiewicz, S. Monnier, G. Cappello, M. Le Berre and M. Piel, *J. Cell Biol.*, 2015, **211**, 765–774.
- 25 P. T. Conduit, K. Brunk, J. Dobbelaere, C. Dix, E. Lucas and J. Raff, *Curr. Biol.*, 2010, **20**, 2178–2186.
- 26 G. Greenan, C. P. Brangwynne, S. Jaensch, J. Gharakhani, J. F. and A. Hyman, *Curr. Biol.*, 2010, **20**, 353–358.
- 27 H. Schatten, *Histochem. Cell Biol.*, 2008, **129**, 667.
- 28 A. Dinarina, C. Pugieux, M. M. Corral, M. Loose, J. Spatz, E. Karsenti and F. Nédélec, *Cell*, 2009, **138**, 502–513.
- 29 M. Ageno, *Nature*, 1965, **205**, 1307.
- 30 N. Bohr and J. A. Wheeler, *Phys. Rev.*, 1939, **56**, 426–450.
- 31 J. D. Bernal and I. Fankuchen, *J. Gen. Physiol.*, 1941, **25**, 111–146.
- 32 Y.-K. Kim, S. V. Shiyankovskii and O. D. Lavrentovich, *J. Phys. Condens. Matter*, 2013, **25**, 404202.
- 33 M. K. Abera, P. Verboven, T. Defraeye, S. W. Fanta, M. L. A. T. M. Hertog, J. Carmeliet and B. M. Nicolai, *Annals of Botany*, 2014, **114**, 605–617.
- 34 T. D. Pollard, *J. Exp. Zool. A Comp. Exp. Biol.*, 2004, **301**, 9–14.
- 35 U. S. Eggert, T. J. Mitchison and C. M. Field, *Annu. Rev. Biochem.*, 2006, **75**, 543–66.
- 36 R. A. Green, E. Paluch and K. Oegema, *Annu. Rev. Cell Dev. Biol.*, 2012, **28**, 29–58.
- 37 J. P. Fededa and D. W. Gerlich, *Nat. Cell Biol.*, 2012, **14**, 29–58.
- 38 A. Khodjakov and C. L. Rieder, *JCB Report*, 2001, **153**, 237–242.
- 39 E. Lifshitz and L. Landau, *Course of Theoretical Physics, volume VI: Fluid Mechanics*, Butterworth-Heinemann, 1987.
- 40 M. Ben Amar, L. J. Cummings and Y. Pomeau, *Phys. Fluids*, 2003, **15**, 2949.
- 41 M. Ben Amar, O. V. Manyuhina and G. Napoli, *Eur. Phys. J. Plus*, 2011, **126**, 19.
- 42 P. Prinsen and P. van der Schoot, *Phys. Rev. E*, 2003, **68**, 021701.
- 43 B. Wincure and A. D. Rey, *Continuum Mech. Thermodyn.*, 2007, **19**, 37.
- 44 M. P. DoCarmo, *Differential Geometry of Curves and Surfaces*, Prentice-Hall, Englewood Cliffs, N.J., 1976.
- 45 O. V. Manyuhina, *Phys. Rev. E*, 2014, **90**, 022713.